

Assessment of the Met Office dust forecast model using observations from the GERBILS campaign

B. T. Johnson,^{a,*†} M. E. Brooks,^{a†} D. Walters,^{a†} S. Woodward,^{a†} S. Christopher^b
and K. Schepanski^c

^aMet Office, Exeter, UK

^bUniversity of Alabama, Huntsville, Alabama, USA

^cUniversity of Leeds, UK

*Correspondence to: B. T. Johnson, Met Office Observation-based Research FitzRoy Road Exeter EX1 3PB United Kingdom E-mail: ben.johnson@metoffice.gov.uk

†The contributions of B. T. Johnson, M. E. Brooks, D. Walters and S. Woodward were written in the course of their employment at the Met Office, UK and are published with the permission of the Controller of HMSO and the Queen's Printer for Scotland.

This paper uses aircraft, ground-based and satellite observations to assess the performance of Met Office dust forecasts during the Geostationary Earth Radiation Budget Intercomparison of Long-wave and Short-wave radiation (GERBILS) campaign. The dust forecasts were produced from a 20 km resolution limited-area numerical weather prediction configuration of the Met Office Unified Model, based over North Africa. Dust uplift was modelled using two modified versions of the Woodward (2001) dust parametrization scheme. The model produced widespread dust over the Sahara desert in response to synoptically driven strong wind events. The modelled aerosol size distribution and short-wave optical properties compared well with aircraft *in situ* measurements and retrievals from the Aerosol Robotic Network (AERONET). Better size distributions and extinction coefficients were achieved by fixing the emitted dust size distribution rather than attempting to predict this dynamically. The two versions performed similarly compared to observations of other variables. The interaction of dust with short-wave and long-wave radiation compared well with aircraft observations when scaled to allow for local differences in Aerosol Optical Depth (AOD). AODs were on average 50–100% too high over south-western parts of the Sahara but 20–50% too low over the Sahel when compared to AERONET sites, aircraft profile estimates and satellite retrieval products. This implicated excessive dust emission over central parts of the Sahara and insufficient dust emissions from the Bodélé depression and semi-arid regions on the southern border of the Sahara. These biases were linked to potential errors in wind speed, soil texture, soil moisture and vegetation, and possible limitations in the dust parametrization, such as the lack of an observationally constrained or geomorphologically based preferential source term. Copyright © 2011 Royal Meteorological Society and British Crown Copyright, the Met Office

Key Words: aerosol; Sahara

Received 6 August 2010; Revised 22 October 2010; Accepted 27 October 2010; Published online in Wiley Online Library 28 January 2011

Citation: Johnson BT, Brooks ME, Walters D, Woodward S, Christopher S, Schepanski K. 2011. Assessment of the Met Office dust forecast model using observations from the GERBILS campaign. *Q. J. R. Meteorol. Soc.* 137: 1131–1148. DOI:10.1002/qj.736

1. Introduction

Dust storms are frequent weather phenomena over deserts and semi-arid regions of the world, leading to disruption and hazards to human health. Dust aerosol also affects the

local, regional and global circulation by altering the fluxes of solar and terrestrial radiation via scattering, absorption and emission. For example, Haywood *et al.* (2005) showed a large bias in outgoing long-wave radiation over south-western parts of the Sahara Desert in comparisons of the

Met Office Unified Model™ (MetUM) with measurements from the Geostationary Earth Radiation Budget (GERB) satellite. This anomaly of up to 50 W m^{-2} was linked to the absence of dust in the operational Numerical Weather Prediction (NWP) model, where Milton *et al.* (2008) also showed errors in the radiation budget of North Africa due to lack of aerosol in the model, leading to excessive solar absorption at the surface and overestimation of surface temperatures. These findings advocate for the representation of aerosols in operational models. Indeed Tompkins *et al.* (2005) and Rodwell (2005) showed positive impacts on the European Centre for Medium-range Weather Forecasts (ECMWF) model following the inclusion of an improved aerosol climatology. The largest changes in Aerosol Optical Depth (AOD) occurred over North Africa but effects on atmospheric circulation were noted, not only on the West African monsoon and African easterly jet, but also on extratropical weather systems of both hemispheres, leading to a notable improvement in the skill of medium-range forecasts. Based on these results a reasonable representation of dust aerosol in models is considered beneficial to forecast accuracy. Moreover, visibility is seriously hampered by high aerosol loadings, and outbreaks of dust pose a major weather hazard in certain dust-prone regions. Therefore prognostic treatment of dust aerosol in NWP models offers valuable forecast information as well as benefits to overall model performance.

In recent years several models have been proposed for the prediction of dust aerosol emissions in global circulation models (Tegen and Fung, 1994; Marticorena and Bergametti, 1995; Alfaro and Gomes, 2001; Ginoux *et al.*, 2001; Woodward, 2001; Zender *et al.*, 2003a). These schemes attempt to simulate the erosion of exposed soil during high winds; a process that occurs via saltation. Saltating sand particles dislodge finer clay and silt particles, which are subsequently lifted into the atmosphere via turbulent air motion. Under this theory there is no explicit consideration for the re-suspension of loose fine particles, or other erosive forces such as vehicles or agricultural activity. In general, atmospheric dust schemes (such as those referenced above) have been developed to assess the role of dust in the climate system, both in past, present and future climates. As such, the overall performance of these schemes is usually judged against long-term climatologies of dust loading and AOD with the goal of reproducing the mean geographic distribution of dust and its seasonal variation. The application to NWP imposes new demands on such schemes to simulate individual dust events to a high degree of accuracy on small spatial and temporal scales. In addition there is a greater stringency in parametrization complexity and computational cost. A simplified parametrization for dust and other major aerosol types was introduced in the ECMWF model as part of the project Global and regional Earth-system Monitoring using Satellite and *in situ* data (GEMS: Hollingsworth, 2005) and accompanied by the data assimilation of AOD from the Moderate-resolution Imaging Spectroradiometer (MODIS). Dust models have also been used operationally in Europe (Nickovic *et al.*, 2001), Australia (Cope *et al.*, 2004), and East Asia (Park and In, 2003; Shao *et al.*, 2003; Tanaka *et al.*, 2003; Uno *et al.*, 2004, 2006) and at the US Naval Research Laboratory (Liu *et al.*, 2003, 2007).

During the Geostationary Earth Radiation Budget Intercomparison of Long-wave and Short-wave radiation

(GERBILS) campaign, a limited-area configuration of the MetUM was run to forecast the meteorology and dust aerosol over the North African region. This limited area model, the Crisis Area Mesoscale Model (CAM) contained almost identical physics to that of the global NWP model and in addition ran a modified version of the Woodward (2001) dust scheme, originally developed by the Met Office Hadley Centre for climate research configurations of the MetUM. The CAM was primarily used as a forecasting tool to aid in flight planning during the GERBILS experiment. However, the simulations also offer a unique opportunity to assess the performance of an operational dust forecasting model against the GERBILS observations. This paper assesses two versions of the dust scheme that were trialled in the CAM. The two versions of the dust scheme differ only in the treatment of dust size distribution. The modelled dust fields are compared against satellite products, *in situ* measurements from the Facility for Airborne Atmospheric Measurement (FAAM) aircraft and retrievals from AERONET.

2. Methods

2.1. The CAM model

The Crisis Area Mesoscale Model (CAM) is a limited-area configuration of the Met Office Unified Model™ (MetUM) used in support of military and disaster relief operations and scientific field experiments (Greed *et al.*, 2008). This is a comprehensive NWP model treating all the relevant meteorological processes. It was run with 20 km horizontal resolution and 38 vertical levels taking boundary conditions from the coarser-resolution operational global NWP MetUM. At this resolution the CAM captures synoptic-scale and mesoscale dynamics well, and parametrizes smaller-scale processes such as convection (Gregory and Rowntree, 1990; Martin *et al.*, 2006) and turbulent mixing (Brown *et al.*, 2008). The model domain for these experiments covers most of North Africa and adjacent portions of the North Atlantic (approx. $0\text{--}40^\circ\text{N}$, $45^\circ\text{W}\text{--}25^\circ\text{E}$, see Figure 1). The radiation scheme is that of Edwards and Slingo (1996) run with six bands in the short wave and nine bands in the long wave.

The CAM was run from 14 to 30 June 2007, allowing 4 days spin-up before the start of the GERBILS period (18–29 June). The dust concentration was set to zero at the initial time and then accumulated with time as the simulation progressed. Analyses showed that the 4-day spin-up period was just sufficient to create a steady balance between dust emission and dust loss via deposition or advection out of the domain. There was no input of dust at the lateral boundaries although dust could exit at the boundaries. Since the wind was generally from east to west this meant that air entering in the east was aerosol-free and air leaving the domain in the west took aerosol with it. The short spin-up and lack of dust input at the boundaries may have both led to an underestimation of background dust, especially of the smaller sizes (bins 1–3) that have longer lifetimes. Although meteorological variables were incremented via data assimilation, the concentration of dust was a free-running variable (not incremented by data assimilation). Since dust was by far the dominant source of observed aerosol mass and optical depth over the GERBILS region (Johnson and Osborne, 2011; Klaver *et al.*, 2011) the

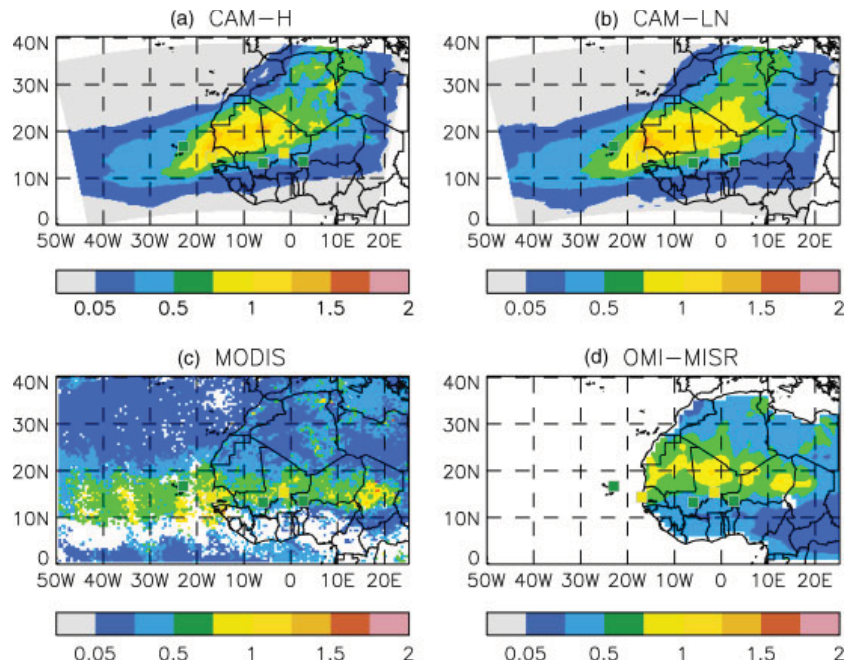


Figure 1. Campaign mean AOD at $0.55 \mu\text{m}$ from the CAM models and satellite data from MODIS and OMI-MISR. Campaign mean AODs from five AERONET sites are plotted as shaded squares. This figure is available in colour online at wileyonlinelibrary.com/journal/qj

representation of other species was not considered essential for this study.

2.2. Parametrization of dust emission and deposition

The dust scheme used in this study was a modified version of Woodward (2001) that has been developed for the Met Office Hadley Centre Earth System Model (HADGEM2-ES). The basis of the scheme is that the emission of dust into the atmosphere arises as a consequence of a horizontal flux of particles across the surface. This horizontal flux is partitioned into nine size bins spanning the size range $0.0316\text{--}1000 \mu\text{m}$, equally spaced on a logarithmic scale, i.e. $0.0316\text{--}0.1$, $0.1\text{--}0.316$, and so on. The horizontal flux (H) is predicted from the surface friction velocity as in Woodward (2001):

$$\begin{aligned}
 H_i &= 0 && \text{for } U^* \leq U_{t,i}^* \\
 H_i &= 2.61\rho(1-\nu)U^{*3} \left(1 + \frac{U_{t,i}^*}{U^*}\right) \left\{1 - \left(\frac{U_{t,i}^*}{U^*}\right)^2\right\} \frac{M_{\text{rel},i}}{g} \\
 \text{for } U^* > U_{t,i}^* &&& H = \sum_{i=1}^9 H_i
 \end{aligned} \quad (1)$$

where U^* is the surface friction velocity over bare soil, $U_{t,i}^*$ is the threshold friction velocity for particles of size bin i , ρ is air density, ν is vegetation fraction, g is gravitational acceleration, and $M_{\text{rel},i}$ is the relative proportion of soil mass composed of particles in size bin i . The influence of subgrid-scale gustiness on surface wind speed is taken into account by increasing the surface friction velocity by a resolution-dependent tuning parameter, i.e. $U^* = C_u \underline{U}^*$, where \underline{U}^* is the original value of surface friction velocity supplied by the surface layer parametrization. C_u takes a value of 1.4 in these simulations. The introduction of the C_u parameter is a modification to the original Woodward

(2001) scheme and the version used in Greed *et al.* (2008). The calculation of threshold friction velocity is also different from the Woodward (2001) scheme and takes the form:

$$U_{t,i}^*(w) = U_{t,\text{dry},i}^* \left[1 + 1.21 \{\max(C_w w - w_t, 0)\}^{0.68}\right]^{\frac{1}{2}} \quad (2)$$

$U_{t,\text{dry},i}^*$ is the threshold friction velocity for nominally dry conditions ($w \leq w_t$), w is the volumetric soil moisture content (m^3/m^3) and C_w is a tuning, which in these simulations was assigned a value of 1. The threshold soil moisture w_t is the residual soil moisture corresponding to the adsorption of water onto the surface of clay particles. This residual moisture is not free to move within the soil and does not contribute to inter-capillary forces that would bind the soil. The threshold soil moisture is given by Fécan *et al.* (1999):

$$w_t = 14F_c^2 + 17F_c \quad (3)$$

where F_c is the clay fraction of the parent soil. $U_{t,\text{dry},i}^*$ is given values: 0.85, 0.72, 0.59, 0.46, 0.33, 0.16, 0.14, 0.18 and 0.28 m s^{-1} , based on Bagnold (1941).

The vertical flux of dust into the atmosphere is assumed to occur only for the smallest six bins (radii $0.0316\text{--}31.6 \mu\text{m}$) and is assumed to be a certain proportion of horizontal flux, as in Marticorena and Bergametti (1995) and the original Woodward (2001) scheme:

$$\begin{aligned}
 G_i &= H \times 10^{((13.4 \min(F_c, 0.2)) - 6)} \\
 &\times M_{\text{sdf},i} \times C_{\text{global}} \quad \text{for } i = 1, 6
 \end{aligned} \quad (4)$$

where G_i is the vertical dust flux and F_c is again the clay fraction. In this version F_c is capped at 20% since this was the highest clay fraction in the measurements of Gillette (1979) on which Eq. (4) is based. The mass in each bin is weighted according to an assumed mass size distribution,

$M_{\text{sdf},i}$ and a global tuning parameter C_{global} . The original Woodward (2001) scheme used in Greed *et al.* (2008) did not include these final terms, i.e. their formulation would be equivalent to assuming $M_{\text{sdf},i} = 1$ and $C_{\text{global}} = 1$. Two alternate assumptions for the mass size distribution were tested in this study. The first approach, referred to as CAM-H, is based on version 2 of the Hadley Centre Environment Model (HadGEM2) and assumes that the shape of the size distribution lifted mirrors that of the smallest six bins within the horizontal flux:

$$M_{\text{sdf},i} = \frac{H_i}{\sum_{i=1}^6 H_i} \quad ; \quad C_{\text{global}} = 1.0 \quad \text{[CAM-H]} \quad (5)$$

The alternative approach, referred to as CAM-LN, assumes that the mass size distribution takes a log-normal distribution, as in Zender *et al.* (2003a):

$$M_{\text{sdf},i} = \frac{1}{2} \left\{ \text{erf} \left(\frac{\ln(r_{\text{max},i}/r_v)}{\sqrt{2} \ln \sigma} \right) - \text{erf} \left(\frac{\ln(r_{\text{min},i}/r_v)}{\sqrt{2} \ln \sigma} \right) \right\} ;$$

$$C_{\text{global}} = 0.3 \quad \text{[CAM-LN]} \quad (6)$$

where r_{min} and r_{max} are the minimum and maximum radii of the size bins, r_v is the geometric volume mean radius, set to 2.91, σ is the standard deviation, set to 1.9, and 'erf' is the standard error function. This reproduces the log-normal mode proposed by d'Almeida (1987) as a fit to their observations of transported dust. The global tuning parameters were set following previous trials to give the best agreement between model AOD and AODs from five dust-prone AERONET sites in the domain (Cape Verde, Dakar, Cinzana, Agafou and Banizoumbou) (see section 2.5). Each model version had to be tuned separately since optical efficiency (extinction per unit mass) and atmospheric residence time vary greatly with particle size distribution. One additional constraint on the dust scheme is that dust emissions are suppressed on steep slopes to avoid anomalous dust production associated with wind speed oscillations around steep orography.

Wet and dry deposition processes follow the same formulation as Woodward (2001) and vary greatly with particle size. For instance, the scavenging coefficient that determines the efficiency of wet deposition varies by a factor of 20 between the small (bins 1 and 2) and large (bins 5 and 6) particles (see Table I of Woodward (2001)). The dominant term in the dry deposition rate is Stokes' velocity, which increases with radius squared. This leads to an order-of-magnitude increase in Stokes' velocity with ascending size bins (since size bins are segregated by a factor of $\sqrt{10}$ in radius). Consequently, the largest particles (bin 6) are removed very quickly by dry deposition (residence times of only a few hours) whereas the small and medium-sized particles (bins 1–4) have long residence times (several days) and are mainly removed by wet deposition.

2.3. Dust optical properties

The optical properties of the dust aerosol were calculated separately for each size bin using Mie theory. Since each size bin covers a wide range of particle sizes (a factor of 3.16) the optical properties were averaged over the size range represented by each bin. The complex refractive index was taken from Balkanski *et al.* (2007), assuming a haematite

content of 1.5%. The results of the Mie calculations were averaged into the six short-wave bands and nine long-wave bands of the MetUM radiative transfer model. The direct radiative effects of the dust were fully coupled to the evolution of the model state. The impact of including this coupling has yet to be explored in the CAM but previous studies with other models (e.g. Heinold *et al.*, 2008) suggest that it can have non-trivial feedbacks on dust emissions. The interaction of dust with cloud condensation nuclei (i.e. indirect aerosol effect) was not represented in this model.

2.4. Aircraft data

The aircraft data used in this study were collected by the Facility for Airborne Atmospheric Measurement (FAAM) aircraft as part of the GERBILS field experiment. This occurred during 18–29 June 2007 over south-western parts of the Sahara Desert (see Johnson and Osborne, 2011, for flight plans and further details). Aerosol size distributions were measured using a Passive Cavity Aerosol Spectrometer Probe (PCASP) and Small Ice Detector. These were calibrated and averaged over all runs during the campaign, as described in Johnson and Osborne (2011). Scattering, absorption, extinction and single-scattering albedos were estimated from the nephelometer and Particle Soot Absorption Photometer (Johnson and Osborne, 2011). AODs were derived by integrating aerosol extinction coefficient over height during vertical profiles. The specific extinction and asymmetry parameters were calculated from Mie theory and T-Matrix calculations using the refractive index data of Balkanski *et al.* (2007) (1.5% haematite) and log-normal fits to the campaign mean aircraft size distribution (Johnson and Osborne, 2011).

2.5. Satellite and AERONET data

AERONET data were obtained from <http://aeronet.gsfc.nasa.gov> for Banizoumbou, Agafou, Institut d'Economie Rurale (IER) Cinzana, Dakar and Cape Verde. We used level 2, version 2 for all AOD and size distribution retrievals that employ the inversion algorithm of Dubovik *et al.* (2006). AOD was interpolated from 0.44 and 0.675 μm to 0.55 μm for comparison against CAM and satellite data. This used logarithmic interpolation. The MODIS data were a combination of the standard collection-5 algorithms for ocean (Remer *et al.*, 2005), dark land surfaces (Levy *et al.*, 2007) and the Deep Blue algorithm for bright surfaces (Hsu *et al.*, 2004). Comparisons with AERONET measurements indicate that standard retrieval meets the expected accuracy levels of $\pm 0.05 \pm 0.15\tau$ over land and $0.03 \pm 0.05\tau$ over ocean ($\tau = \text{AOD}$). Comparisons between the Deep Blue and AERONET AODs are generally within 20–30% of each other (Hsu *et al.*, 2004). All three of these products are at a nominal spatial resolution of $10 \times 10 \text{ km}^2$ but have been averaged to generate a 0.5×0.5 degree mean AOD over the area of study.

The OMI-MISR AOD product combines Multi-angle Imaging SpectroRadiometer (MISR) AOD with the Ozone Monitoring Instrument (OMI) Ultraviolet Absorbing Aerosol Index (OMI AI), as outlined in Christopher *et al.* (2008). This product has already been used for model verification and validation (Greed *et al.*, 2008). Due to its narrow swath width, MISR cannot provide daily maps of AOD over the entire Saharan region. In order to take

advantage of the OMI AI data where daily values are available for the entire study region, AI is converted into AOD values using relationships between OMI AI and MISR AOD at 0.5×0.5 degree resolutions. The estimated AOD compared within 20% of the AERONET AODs in dust regions (Christopher *et al.*, 2008).

3. Validation of model AOD

3.1. Campaign mean spatial distribution of AOD

The performance of the dust simulation has been examined by comparing the dust AOD from the model against various sources of observational data. Figure 1 shows the campaign mean AOD at $0.55 \mu\text{m}$ from CAM-H, CAM-LN and the MODIS and OMI-MISR satellite products. The campaign mean AOD from five AERONET sites (interpolated from 0.44 and $0.675 \mu\text{m}$ to $0.55 \mu\text{m}$) are over-plotted in square boxes. Both models produce widespread dust over the Sahara with AODs ranging from 0.25 to 1.5 over a broad portion of the continent. The AOD patterns in CAM-H and CAM-LN are similar though with some subtle differences. For example CAM-H has a slightly higher degree of heterogeneity than CAM-LN.

The models are both in broad agreement with the range of AODs in the satellite products, although there are obvious discrepancies in the geographic distribution. The models develop the highest AODs in a single large plume extending from Algeria through to the Atlantic coast. AODs peak at around 1.5 at the centre of these plumes. In contrast, MODIS has the highest AODs in a belt running east–west between 10 and 20°N and a peak of around 1.5 over Chad. OMI-MISR has maximum AODs further north (15 – 25°N), closer to where the model produces the highest AODs although it has few peak AODs over 1 . There is therefore some uncertainty over the north–south position of maximum AODs, and this shows up well when comparing zonal mean AODs (Figure 2). The reason for this disagreement is not clear but the strong north–south gradients in surface reflectivity and aerosol optical properties are likely to be major challenges for any satellite retrieval in this region. The AERONET data (see Table I), though spatially limited, agree better with MODIS than OMI-MISR. For example, there is a large discrepancy between AERONET and OMI-MISR AOD at Cinzana (12°N , 6°W). Figure 2 and the AERONET data (Table I) therefore suggest that the models have the dust too far north and too little AOD in the Sahel (south of 15°N). The problem may relate to insufficient dust south of 15°N or the lack of other relevant aerosol species (e.g. anthropogenic, natural biogenic) that were not represented in CAM. The models inevitably underestimate AOD in eastern parts of the domain due to a lack of incoming dust at the model boundaries. This problem seems to be compounded by insufficient dust emissions from Chad (Figure 1, and discussed in section 4). This low bias in the east is quite clear when comparing FAAM profile AODs with co-located model AODs (Figure 3). Conversely, at the western end of the aircraft operating region the model quite clearly overestimates AOD. This is supported by the AERONET data at Dakar where the model AOD is a factor of 1.5 – 1.8 too high (see Table I). Thus, the main plume of dust in the models is too strong but other plumes (i.e. those originating from Chad and the Sahel border $\sim 15^\circ\text{N}$) are too weak.

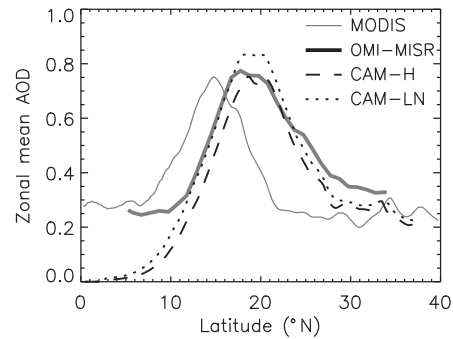


Figure 2. Campaign mean zonal mean AOD at $0.55 \mu\text{m}$ averaged over the longitude range 20°W – 20°E for MODIS, OMI-MISR, CAM-H and CAM-LN.

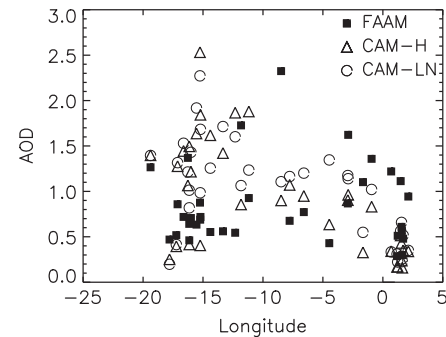


Figure 3. AODs at $0.55 \mu\text{m}$ from FAAM aircraft profiles and co-located model output from CAM-H and CAM-LN.

The comparison of model AOD with MODIS suggests that long-range transport of dust over the Atlantic may have been insufficient in the models. The belt of high AODs (>0.5) between 10 and 20°N extends all the way from the African coast to about 45°W in the MODIS data. The models only bring this tongue of high AODs out as far as 30°W , about half the distance shown by MODIS. The neglect of sea salt aerosol in the model muddies this comparison but only to a small extent. Time series of MODIS images suggested that high AODs (>0.5) over the ocean were exclusively associated with aerosol plumes originating over Africa. The vast majority of dust deposition events during these simulations occurred via dry deposition rather than wet deposition, thus implying that the gravitational settling rate and/or surface layer deposition flux may be too high in the model. Assessing this in detail is beyond the scope of this study.

3.2. Validation of AOD during a large dust event

A large dust storm occurred on 20–21 June 2007 bringing AODs of over 1.5 to large swathes of West Africa. The dust storm was driven by a synoptic-scale high-winds event over central parts of the Sahara on 20 June that subsequently swept down over southern Mali and Senegal on 21 June. The event was well captured by infrared imagery from the Spinning Enhanced Visible and Infrared Imager (SEVIRI) (Figure 4, shows dust as pink), the Aerosol Index product from OMI and the AOD retrievals from MODIS (Figure 5). AERONET AODs at Dakar and Cinzana showed marked increases from less than 0.5 on 19 June to over 1.5 on 21 June (Figure 6).

Table I. Campaign mean AODs at 0.55 μm at five AERONET sites

	Cape Verde	Dakar	Cinzana	Agafou	Banizoumbou
Lat, lon ($^{\circ}$)	16.7N, 22.9 W	14.4N, 17.0 W	13.3N, 5.9 W	15.3N, 1.5 W	13.5N, 2.7E
AERONET	0.50	0.76	0.88	0.86	0.62
MODIS	0.62	0.64	0.70	0.73	0.56
OMI-MISR	n/a	0.63	0.37	0.60	0.51
CAM-LN	0.64	1.08	0.58	0.60	0.30
CAM-H	0.63	0.99	0.44	0.50	0.21

Figure 7 shows the high-winds event as represented by the CAM model wind fields and the associated intense dust emissions. The dust storm is generated by strong north-easterly surface winds over the central Sahara and is then transported by a coherent east to north-easterly flow at mid-levels. A FAAM aircraft flight on 21 June showed the dust layer over southern Mali to be mainly located between 2 and 4.5 km altitude (see section 7) so we have assumed the 3 km wind to be a good guide to the steering flow. The initial hot spot of high dust AOD in the CAM on 20 June corresponds well to the location of the emerging dust storm shown by the MODIS, OMI and SEVIRI plots (Figures 4 and 5). The CAM also produces a fair amount of dust on 21 June as the high surface winds move further southwest. Diffluent flow at mid-levels then strains the plume creating a plume with a large head over Senegal and an elongated tail running back into Mali. The general shape of the dust plume is well captured by CAM (Figure 5) but its position is slightly too far north. This was confirmed by the aircraft observation made by the FAAM aircraft (see section 7) and also by the underestimation of AOD at Dakar and Cinzana (Figure 6).

The CAM therefore seems to do a fairly good job at capturing the dynamics and dust uplift during synoptically driven dust events. However, errors in either the geographic distribution of dust sources (see section 4) or surface friction velocity lead to poor skill in forecasting the AOD at specific locations. The fact that the dust plume was too far north in the model again shows that the model may not lift sufficient dust in the semi-arid regions of the Sahel.

4. Dust emissions

Figure 8(a) shows the geographic distribution of dust emissions from CAM-H averaged over the campaign period (18–29 June 2007). This is the total mass of dust emitted over all size bins (i.e. the total vertical flux, G). The geographic distribution of emissions from CAM-LN (not shown) was virtually identical to that of CAM-H but a factor of ~ 4 lower. This difference in total emission was mainly due to the lower global tuning parameter (Eqs (5) and (6)). However, feedbacks between the dust loading, its radiative effects and the model wind fields apparently had some influence on the total dust emission, otherwise the ratio of CAM-H to CAM-LN total emissions would have been exactly (1:0.3) or 3.33. This potential feedback mechanism has not been investigated here but may be of interest for future studies. The dust emissions were widespread over desert areas to the north of 15 $^{\circ}$ N but emission rates were very inhomogeneous, varying from 0 to 30 $\text{g m}^{-2} \text{d}^{-1}$. The highest emission rates were found in western regions of the

Sahara. For ease of reference, Figure 8(b) shows the model orography, with labelled countries and geographic features.

While no direct observations of dust emission rate are currently available for comparison against the model emission field, the Dust Source Activation Frequency (DSAF) derived from SEVIRI observations by Schepanski *et al.* (2009) provides for a qualitative assessment. Figure 8 shows the DSAF for June, July and August (JJA) 2007 (Figure 8(c)) and the annual mean for the years 2007 and 2008 (Figure 8(d)). The DSAF was derived by tracking every observed dust event back, through the 15-minute SEVIRI observations, to the first observed source (Schepanski *et al.*, 2007), and these dust source observations are accumulated on a daily basis onto a $1^{\circ} \times 1^{\circ}$ grid. The DSAF is therefore the proportion of days during the period which a particular $1^{\circ} \times 1^{\circ}$ grid box is observed to be an active dust source. While DSAF does not translate directly into an estimate of the dust emissions, the spatial patterns of the emission rate and DSAF should be well correlated. The CAM-H emission pattern shares some of the broader features of the DSAF for JJA 2007 although there are some exceptions to this agreement. The main discrepancy is that the emissions appear to drop to zero at roughly 2° to 4° too far north, missing out the Air Massif at 16 $^{\circ}$ N 8 $^{\circ}$ E. When looking in more detail, other discrepancies include the high CAM-H emissions along the Moroccan coast that do not appear in the DSAF observations and high DSAF in the region of the Bodélé depression (15–18 $^{\circ}$ N, 15–20 $^{\circ}$ E) and the southern tip of Algeria that are not strongly reflected in CAM-H. The lack of observed dust sources on the Moroccan coast may be due to the presence of cloud, and reduced brightness temperature differences along the coast. However, any further investigation would also need to consider whether the high wind speeds along the Moroccan coast are realistic in the model (see section 4.2). The comparison of details such as these may be highly influenced by the variability of synoptical-scale meteorology, given the short model simulation period (12 days from 18 to 29 June 2007). However, because surface characteristics place a strong constraint on where dust may or may not be emitted (both in reality and in the model) useful insights may still be gained from the comparison. For example, the model dust emissions do not seem sensitive to the orography within the interior of the Sahara. The dust sources associated with the depression in central Algeria (26 $^{\circ}$ N, 2 $^{\circ}$ E) are not reflected in the CAM-H emission pattern, and the model fails to sufficiently inhibit emissions over the Hoggar mountains (26 $^{\circ}$ N, 6 $^{\circ}$ E). The DSAF shows some support for the regions of low or zero emissions in the interior of the Sahara that the model predicts. As explained below, these are associated with a lack of clay at the surface.

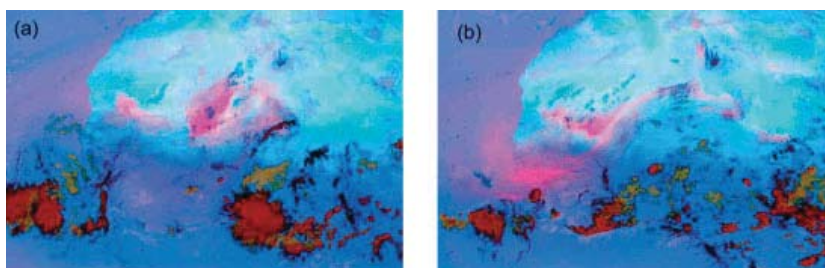


Figure 4. SEVIRI infrared dust images for 1400 UTC on (a) 20 and (b) 21 June 2007.

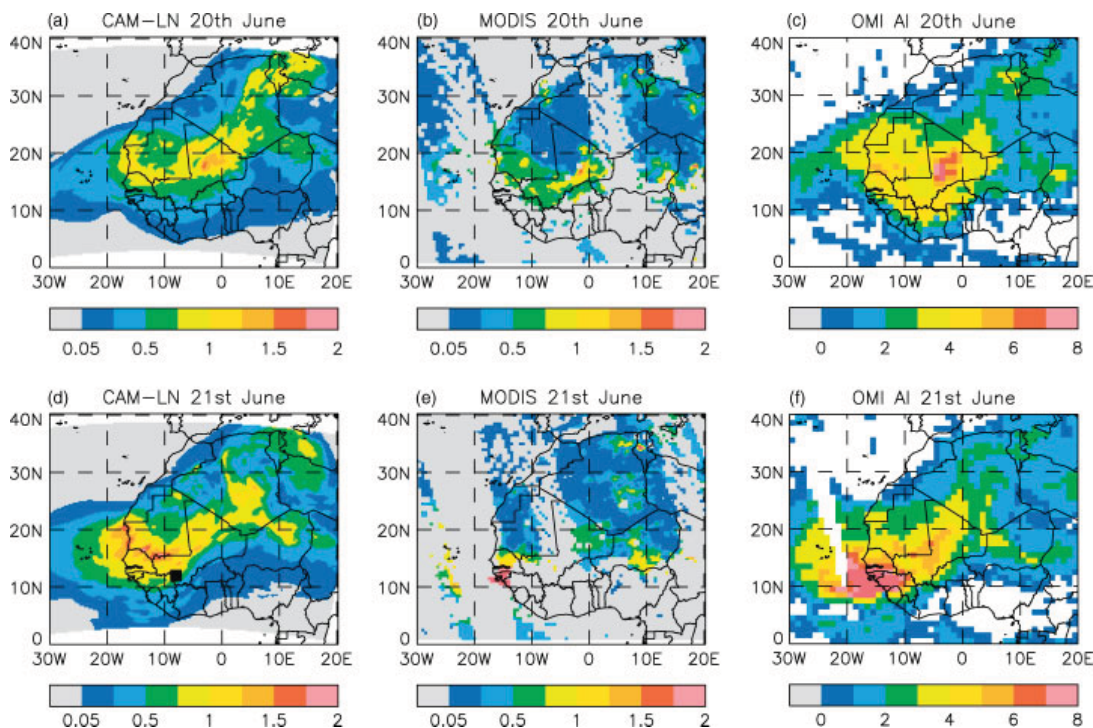


Figure 5. CAM-LN AOD, MODIS AOD and OMI Aerosol Index for ~1400 UTC on 20 and 21 June 2007. The location of a FAAM profile on 21 June is shown by the black square in the CAM plot. This figure is available in colour online at wileyonlinelibrary.com/journal/qj

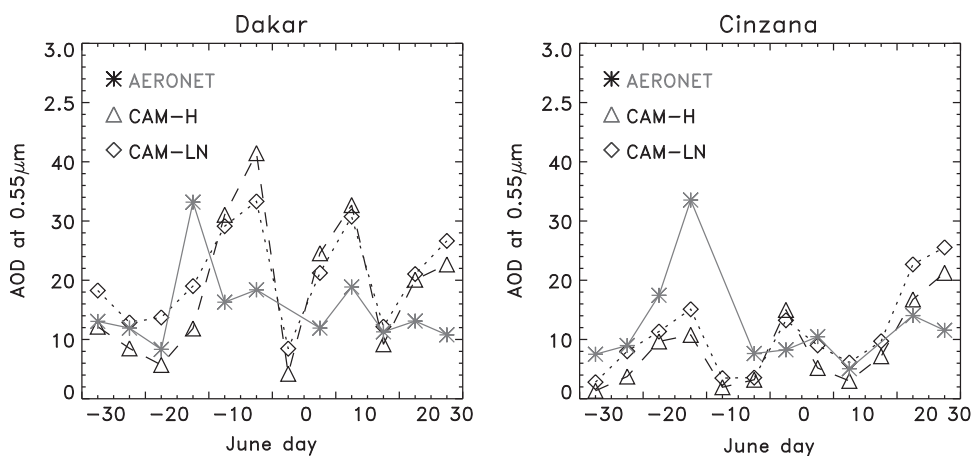


Figure 6. Daily AODs at $0.55 \mu\text{m}$ from the CAM models' 1200 UTC analyses and AERONET retrievals averaged from 1000 to 1400 UTC at Dakar and Cinzana in June 2007.

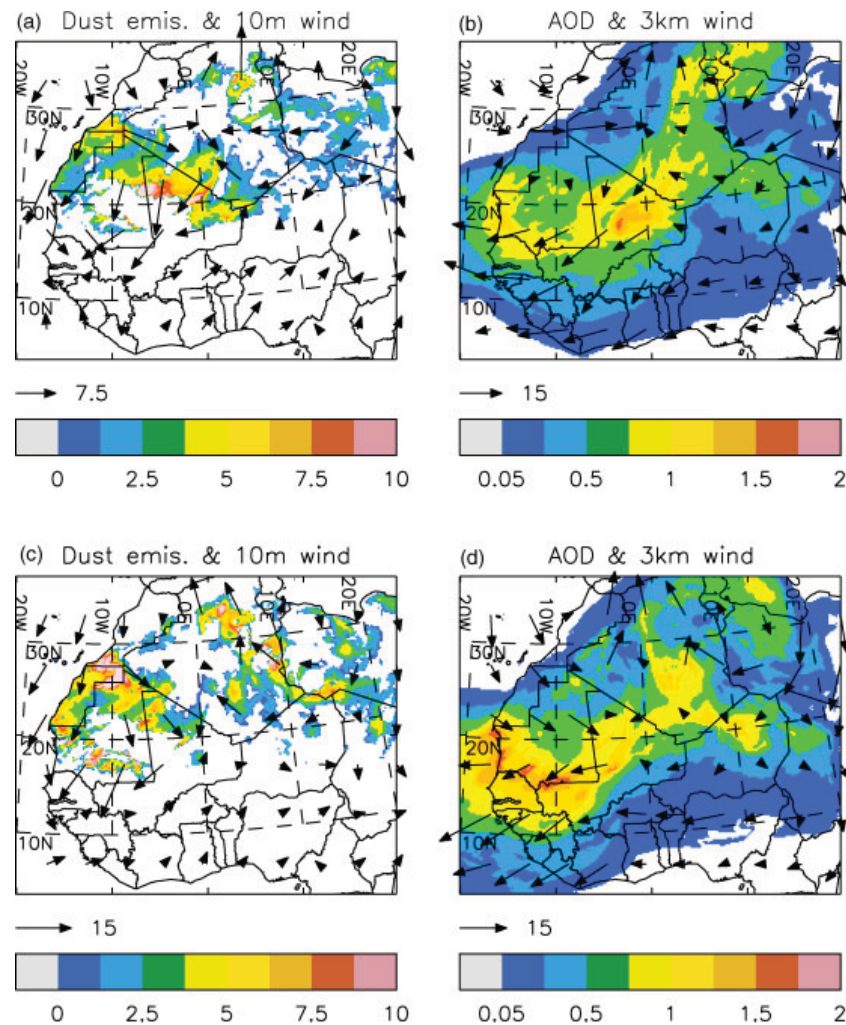


Figure 7. Dust emission ($\text{g m}^{-2} \text{d}^{-1}$) and 10 m wind vectors, AOD and 3 km wind vectors for 1200 UTC on (a and b) 20 June and (c and d) 21 June 2007 for the CAM-LN simulation. This figure is available in colour online at wileyonlinelibrary.com/journal/qj

4.1. Relationship of dust emissions to surface properties

The rate of dust emission depends on several properties of the land surface including soil composition, soil moisture and vegetation cover. In this section we explore how well these factors are treated in the model and how the formulation of the parametrization affects the behaviour of emissions.

The soil clay fraction is a strong limiter of dust emission, as shown in Figure 9(b), based on Marticorena and Bergametti (1995), using only seven observations from Gillette (1979). Emissions increase very rapidly with clay fraction until clay fraction reaches 20%, then the curve flattens off, as expected due to the 20% cap on the F_c term in Eq. (4). The exponent in Eq. (4) leads to a factor-of-100 difference in emission rates between areas of low (5%) and high ($\geq 20\%$) clay fraction. Figure 9(a) shows the clay fractions used in the CAM, generated from the International Geosphere–Biosphere Programme (IGBP) land cover and soil dataset (Loveland and Belward, 1997; Global Soil Data Task Group, 2000). This shows that the majority of land areas in the domain have clay fractions of 20% so the clay fraction term of the parametrization only limits emissions in a few regions. These irregular-shaped regions of low clay fraction explain

the ‘holes’ in the emission field (Figure 8(a)) (i.e. patches of negligible or zero emission) in the interior of the Sahara.

The spatial patterns of these emission holes in Figure 8(a) are best compared to the 2007–2008 annual mean DSAF (Figure 8(d)). By averaging over this wider time period, Figure 8(d) gives a statistically more robust indication of which regions within the Sahara are not active dust sources. The largest feature is an area of low annual mean DSAF spanning central Mauritania and northwestern Mali. This corresponds, albeit roughly, to the areas of low clay fraction in the IGBP dataset and is a reflection of the large expanses of sand dunes in those regions. Similar correspondence is seen between the emission holes in western Algeria and western Libya and areas of low annual mean DSAF. By contrast there are a number of smaller clay fraction emission holes in northern Algeria which all miss a small region of low DSAF. Looking at southern Algeria, Niger and Chad, there are several regions of very high annual mean DSAF – the Bodélé depression in Central Chad and drainage flows/wadis from the highlands of the Hoggar in Southern Algeria, the Air just to the south in Niger and the Tibesti in northern Chad. Between the Air, Tibesti and Bodélé there is a region of slightly lower DSAF in the sand dunes of the Grand Erg de Bilma in eastern Niger. From Figure 9(a) the Grand Erg

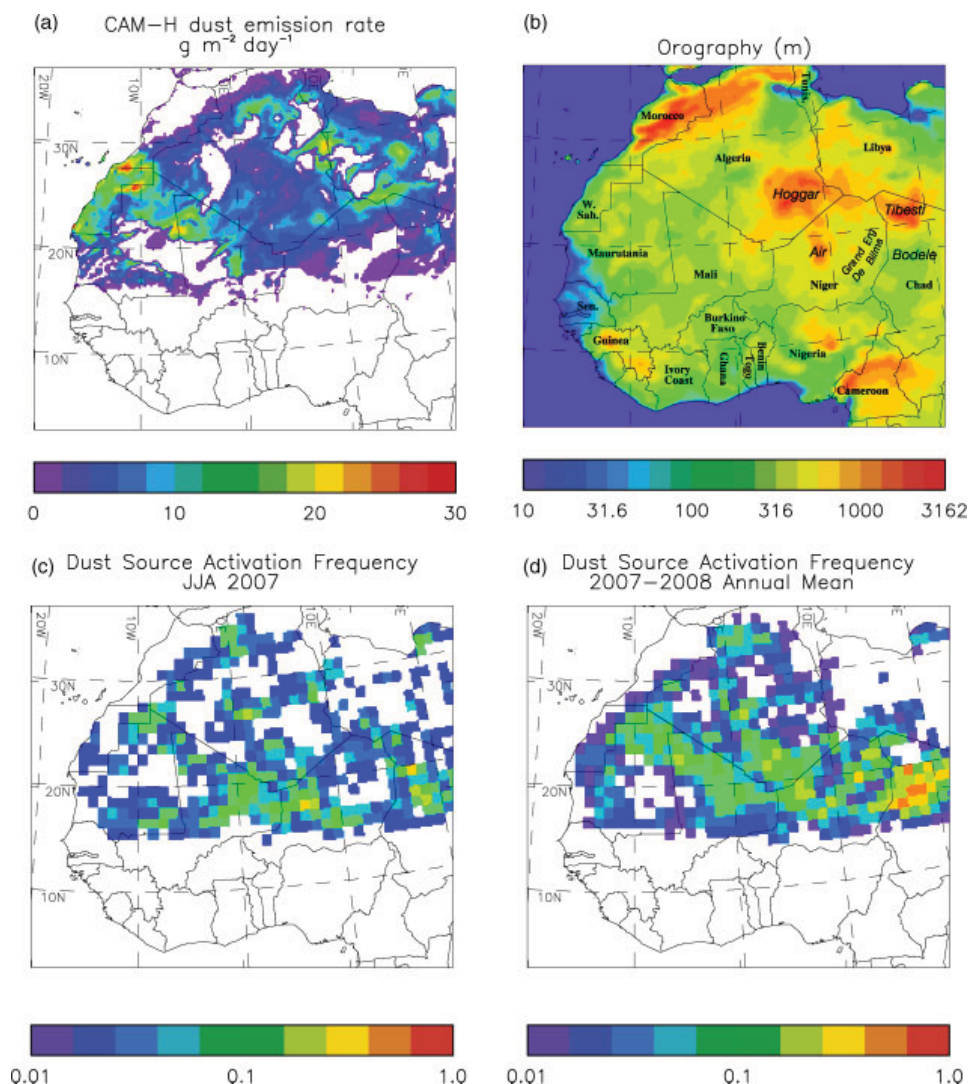


Figure 8. (a) Campaign mean dust emissions from CAM-H model with (b) labelled model orography. For comparison, the Dust Source Activation Frequency (DSAF) from SEVIRI observations for 2007–2008 (Schepanski *et al.*, 2009) is shown for (c) June, July and August 2007 and (d) 2007–2008 annual mean. This figure is available in colour online at wileyonlinelibrary.com/journal/qj

de Bilma shows no dust emission and the Bodélé region has a modest level of emission in comparison to the annual mean and JJA DSAF. The weak or modest emissions in those regions were in part due to a lack of strong wind events during the simulation period (see Figure 12(a)). However, the clay fraction in the Bodélé region is lower than 20% (i.e. below the cap on F_c applied in Eq. (4)) and this shows that emissions would have been inhibited in that region even though it is known to be one of the most intense dust source regions in the world (e.g. Washington *et al.*, 2006). The Air and Tibesti are just outside the region of low clay fraction. This shows either a need to examine the soil clay fraction dataset or the theory linking dust emission to clay fraction.

Other soil datasets were examined, such as a new high-resolution soil texture map from Dharsri (2010) that merges data from the Harmonised World Soil Database (FAO, 2008), State Soil Geographic Database (conterminous USA region, Miller and White, 1998) and point observations of soil sand, silt and clay fractions, and while the details within the regions of high clay fractions were noticeably different, the regions of low clay fraction were found to be identical

(not shown). A re-examination of the relationship between dust vertical flux and clay fraction may be necessary. For example, given the uncertainties in the original analysis (Gillette, 1979) it could be argued that the relationship in Eq. (4) does not hold well for $F_c > 10\%$. Reducing the cap on the F_c term in Eq. (4) would greatly reduce the dependency of dust emission on clay fraction and might resolve some of the problems shown above. However, a more fundamental problem that would also need resolving is lack of representation for bare rock in the model. An additional issue is also to examine whether the theory of particle release via saltation and attrition is an adequate description for how dust is emitted in all environments. Addressing this later problem is a topic for further research.

The vegetation and soil moisture place additional strong constraints on dust emissions from around 15°N southwards (Figure 10). In this transition zone, bare soil fraction decreases from 100% in the Sahara to less than 10% in the Sahel across a very narrow region of only 100–300 km (Figure 10(a)). Unlike some of the Met Office climate models which have an interactive vegetation fraction, the vegetation

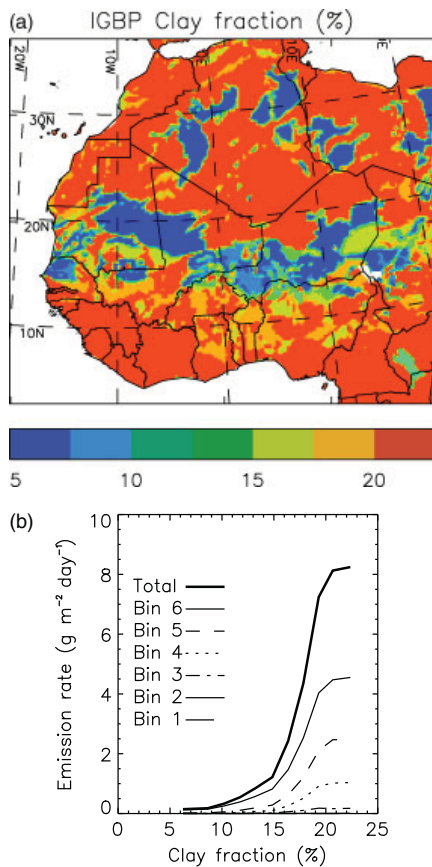


Figure 9. Soil clay fraction and mean dust emission rate from CAM-H as a function of soil clay fraction. This figure is available in colour online at wileyonlinelibrary.com/journal/qj

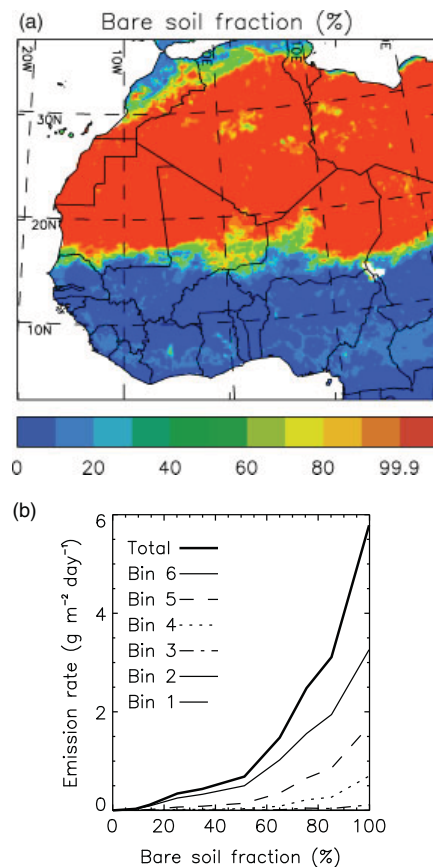


Figure 10. Bare soil fraction and mean dust emission rate from CAM-H as a function of bare soil fraction. This figure is available in colour online at wileyonlinelibrary.com/journal/qj

fraction in the CAM is prescribed and does not vary with time. Seasonal vegetation die-back is represented by the evolution of a leaf-area index term, which is prescribed from a monthly climatology derived from MODIS observations (Knyazikhin *et al.*, 1999). This formulation works well in describing the seasonal variability of surface albedo but there is currently no link from this to changing the exposure of the soil to the wind. In the CAM dust scheme the relationship between dust emission and vegetation is the fraction given by the $(1 - v)$ term in Eq. (1) preventing dust emission over vegetated areas (Figure 10(b)). As a consequence of this, CAM-H is unable to emit dust in the seasonally vegetated Sahel, while the annual mean DSAF observations clearly shows that dust emission does occur in this transition zone, particularly in the Air mountains which are in a region of 50% vegetation.

Soil moisture also increases from 4% or less in the Sahara to 15% or more across a more gradual transition zone (Figure 11(a)). This more gradual transition zone means that the soil moisture does not produce the unrealistic constraints to the dust emission which are caused by the vegetation fraction term. The relationship between dust emission and soil moisture is shown in Figure 11(b). The average emission rate falls rapidly as soil moisture exceeds 4% and drops to zero where soil moisture exceeds 14%. The slight increase in dust emissions with soil moisture from soil moisture values of 1–4% is counter-intuitive but clearly demonstrates the threshold nature of the relationship; the soil only needs to be ‘dry enough’. In this model simulation,

‘dry enough’ corresponds to $w \sim 4\%$ (as can be expected by substituting $F_c = 0.2$ in Eq. (3)).

The CAM-H model size distribution changes dramatically with increasing soil moisture; the smaller size bins are suppressed much more strongly by moisture than the larger size bins. This is because the smaller size bins have higher threshold friction velocities so a little extra soil moisture may increase the threshold friction velocity beyond friction velocity values diagnosed by the model (see Eq. (2) in section 2.2). The consequence is that only the heaviest size bin (bin 6, 10–31.6 μm) is lifted once soil moisture exceeds 7% and very skewed source size distributions occur in CAM-H across the semi-arid zone. In CAM-LN the source size distribution was universally fixed (Eq. (5)) so did not vary with any of the above factors. However, the total mass emission from CAM-LN responded to soil texture, soil moisture and vegetation in exactly the same way as CAM-H. This is because the total dust emission (vertical flux) is related to the horizontal flux in the same way in both model versions (Eq. (4)), the only difference between the two schemes being a change in the source size distribution and global tuning parameter. Hence the equivalent CAM-LN plots are not shown.

4.2. Relationship of dust emission to wind speed

The wind speed is another very important factor in determining dust emission. Since dust emission increases with the cube of wind speed, it is important to get both

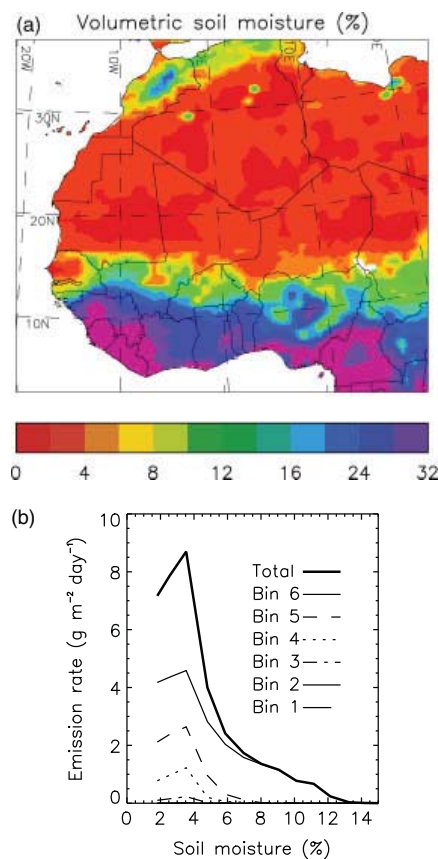


Figure 11. Campaign mean volumetric soil moisture content (water vol./soil vol.) and mean dust emission rate from CAM-H as a function of soil moisture content. This figure is available in colour online at wileyonlinelibrary.com/journal/qj

mean and peak wind speeds right. In this study we do not make a full assessment of the model wind fields but consider how the mean surface wind affects the pattern of emissions. We also consider how the formulation of the parametrization affects the relationship between wind speed, dust emission and emitted size distribution.

Over areas of dry, bare, clay-rich soils, dust emissions were driven primarily by surface wind speed. Although the parametrization is written in terms of friction velocity (U^*), it is more intuitive to consider how dust emissions vary with the 10 m wind speed (Figure 12(a)). Since the model assumes a uniform roughness height over all bare soil surfaces, U^* and the 10 m wind speed were well correlated in the model. The highest mean surface winds occurred over western parts of the Sahara and locally in some northern parts of the Sahara. These areas of peak wind speed correspond well with areas of maximum dust emission shown in Figure 8. As Figure 12(b) shows, there is a strong relationship between 10 m wind speed (U_{10m}) and dust emissions rate. Dust emissions begin when the 10 m wind speed exceeds 3 m s^{-1} and grew nonlinearly due to the cubic dependence of U^* (see Eq. (1) in section 2.2). The threshold at 3 m s^{-1} corresponded to surface friction velocities exceeding the threshold value ($U^*_{t,dry}$) for size bin 6. In CAM-H the smaller size bins are only lifted at high wind speeds (e.g. bin 3 only for $U_{10m} > 9 \text{ m s}^{-1}$) leading to a gradual shift in the size distribution with increasing wind speed. In CAM-LN the source size distribution was fixed (see section 5)

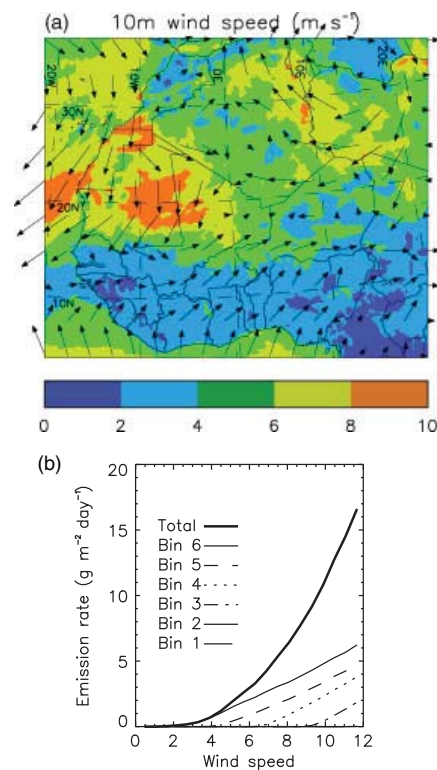


Figure 12. Campaign mean 10 m wind speed, with wind vectors and mean dust emission rate from CAM-H as a function of 10 m wind speed (m s^{-1}). This figure is available in colour online at wileyonlinelibrary.com/journal/qj

but the total mass emission followed the same pattern as in CAM-H (not shown). Therefore CAM-LN emitted all sized particles for $U_{10m} > 3 \text{ m s}^{-1}$ whereas CAM-H requires much greater wind speeds to emit long-lived and optically efficient particles (i.e. bins 1–4).

Figure 12(a) also shows a general drop in wind speed between the desert and vegetated zone south of 15°N . This drop in 10 m wind speed was partly due to the drag exerted by vegetation; the ratio of 10 m wind speed to 925 hPa speed was almost 1 over desert and nearer 0.5 over vegetated regions (not shown). Thus vegetation suppresses dust emissions indirectly, by retarding the wind, as well as directly via the $(1 - v)$ term in Eq. (1). In theory the drag exerted by vegetation, due to its higher roughness length, would increase turbulence and increase the ratio of U^* to U_{10m} . However, the model diagnoses U^* independently for each surface type, according to the roughness length specified for that surface. This implicitly assumes that areas of bare soil are separate from, and not influenced by, the roughness of other surfaces within the grid box, except via their effects on grid-box mean wind speed. This assumption is necessary whilst the model does not have a representation for the interaction of wind with the surface in areas of mixed vegetation and bare soil. The model may also poorly represent certain mechanisms that can generate high winds at low levels. These include the diurnal cycle of mixing of momentum from nocturnal low-level jets to the surface (e.g. Todd *et al.*, 2007; Schepanski *et al.*, 2009), the monsoon flow (Bou Karam *et al.*, 2008) and cold-pool outflows from deep convection (e.g. Knippertz *et al.*, 2007). These are all expected to be important processes (Marshall *et al.*, 2008a; Bou Karam *et al.*, 2009; Marticorena *et al.*, 2010) but

their relative contributions are currently poorly understood. Furthermore, subgrid variations in wind were not accounted for in the model except through a resolution-dependent tuning of the surface friction velocity, which assumes a uniform gustiness everywhere rather than attempting to parametrize the effects of processes such as boundary-layer convection (Marshall *et al.*, 2008b), dust-devils (Koch and Renno, 2005), and downdraughts from moist convection.

5. Aerosol size distributions

5.1. Domain mean size distributions

The size distribution of dust is important for both the interaction with radiation and the rates of wet and dry deposition. However, the size distribution varies greatly with space and time and spans at least 2–3 orders of magnitude. The CAM dust scheme segregates dust particle size into six size bins spanning the range 0.0316 to 31.6 μm . Whilst CAM-H predicts the size distribution of emitted particles from size-dependent threshold friction velocities, CAM-LN simply specifies this as a log-normal function, as explained in section 2.2. CAM-H leads to highly skewed initial size distributions with the mass emissions increasing rapidly with increasing particle size (Figure 13(a)). This is due to the decrease of threshold friction velocity with increasing particle size. Thus much stronger winds are required for lifting of the smaller particles. The CAM-LN size distribution peaks in bin 4 ($r \sim 2 \mu\text{m}$) and has a very small contribution from the largest size bin, in stark contrast to the result from CAM-H. The log-normal used to specify this distribution was based on observations of transported dust, i.e. in situations where large particles would have dropped out with time. The total emissions from CAM-H are about 4 times higher than from CAM-LN due to the higher global tuning parameter (C_{global}) in Eqs (5) and (6) (section 2.2). However, because the large particles fall out quickly, the size distribution and total mass loading in the atmosphere, remote from sources, are quite similar in CAM-LN and CAM-H (Figure 13(b)). The large particles also have very low optical efficiency. Together these two reasons explain why AODs were similar from each model, despite the factor-of-4 difference in total mass emissions (sections 3 and 4).

5.2. Comparison of size distribution with observations

The modelled size distributions have been validated against observations from the FAAM aircraft and retrievals from the AERONET (Figure 14). The FAAM data give a campaign mean averaged over all aircraft runs in dust layers which covered a fairly representative range of altitudes, so the campaign mean constitutes our best estimate of the typical size distribution over the GERBILS region (Johnson and Osborne, 2011). The AERONET retrievals are column means at the Dakar and Banizoumbou sites, averaged over all retrievals during the period 18–29 June 2007. The two AERONET size distributions are very similar and agree fairly well with the aircraft data with $dV/d(\log r)$ peaking at radii of around 1.5–2.5 μm . To compare with the CAM we averaged all model data between 0900 and 1500 UTC during 18–29 June for the grid boxes over Dakar and Banizoumbou to reflect the typical temporal coverage of the AERONET and flight data. All model and observed curves are normalized

to give a value of 1 when integrating over $d(\log r)$ to avoid confusion due to differing total concentrations.

Comparing the CAM-H and CAM-LN size distributions in Figure 14 shows that the CAM-LN appears to match the observations more closely, having a peak centred on bin 4 (radius of 1–3.16 μm) with roughly the correct variance. CAM-H gives a broader peak with much higher concentrations in bin 5 (3.16–10 μm). This leaning towards larger particles leads to poorer agreement with the GERBILS observations. However, given the uncertainty in the observed size distribution (Johnson and Osborne, 2011) and the natural variability of dust size distribution, the CAM-H size distribution should still be considered a realistic result. The bias towards the larger particles might also be a product of errors in U^* , soil moisture and the tuning parameters, all of which affect the emitted size distribution. Thus, the CAM-H size distribution formulation (Eq. (5)), though more physically justified, adds an additional level of sensitivity to the dust model, adding to the need for careful tuning and attendance to other model errors. CAM-H also leads to greater variability in the size distributions as shown by the greater proportion of bins 5 and 6 particles found at Banizoumbou than at Dakar. This is partly because the emitted size distributions vary with wind speed and soil moisture, and partly because more of the dust mass is associated with bins 5 and 6 that have fast deposition rates. This greater degree of spatial and temporal variability may be an advantage of CAM-H in applications where contrast is a desirable feature in the forecasts.

6. Short-wave aerosol optical properties

The CAM aerosol optical properties were calculated for each size bin from Mie theory using the refractive index data from Balkanski *et al.* (2007). To calculate optical properties corresponding to the whole size distribution we integrated over all size bins, weighting by the column burden in each size bin. FAAM aerosol optical properties were either measured directly or calculated by Mie theory and T-Matrix spheroids using the Balkanski *et al.* (2007) refractive index and the campaign mean size distribution (Figure 14). The AERONET optical properties of single-scattering albedo, Ångström exponent and asymmetry parameter were taken from the inversion retrievals (Dubovik *et al.*, 2006, see section 2.5). The AERONET specific extinction coefficient was derived by dividing the retrieved AOD by the retrieved aerosol column volume and then dividing by an assumed aerosol density of 2.65 g cm^{-3} . The averaging approach used to calculate campaign means was the same as in section 5.2. The CAM regional mean corresponds to the area (10–25°N, 20°W–5°E). All values are given in Table II.

The model aerosol optical properties generally agree quite well with the observations. For example, the single-scattering albedo, asymmetry parameter and Ångström exponents are all within the range and uncertainty of the observations. This is a major improvement over previous versions of CAM (Greed *et al.*, 2008) that had very large errors in optical properties (e.g. Ångström exponents of around 0.9) due to excessive proportions of fine particles. The overall agreement in single-scattering albedos is good due to good size distributions and a good refractive index source (Balkanski *et al.*, 2007). These new refractive index data replace the values used in the original Woodward (2001) scheme and are more consistent with AERONET and recent

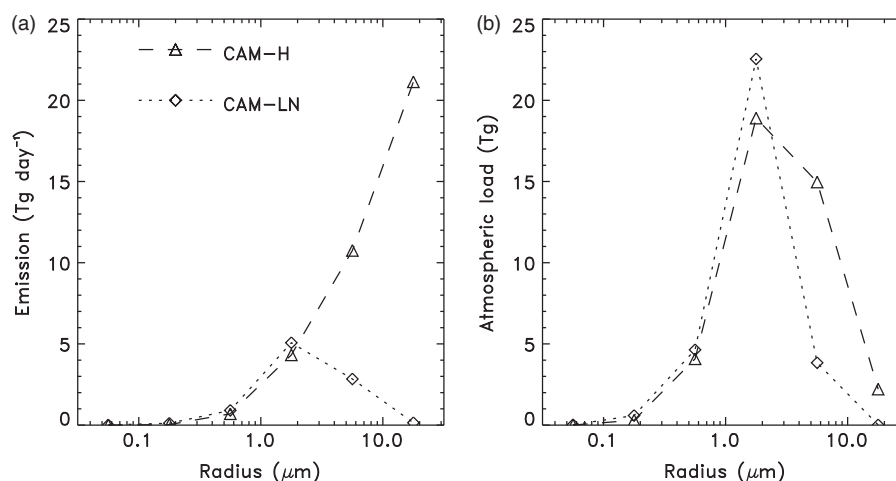


Figure 13. Campaign mean domain mean size distributions of (a) dust emission and (b) atmospheric loading from the CAM-H and CAM-LN models.

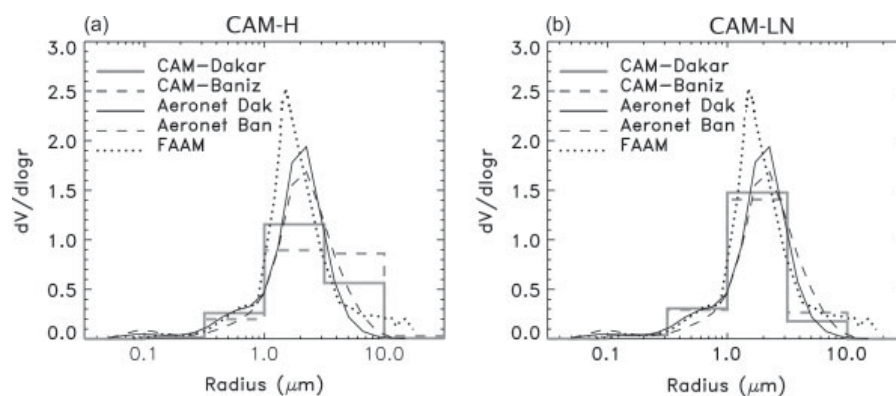


Figure 14. Campaign mean aerosol size distributions from FAAM aircraft, CAM and AERONET at Banizoumbou and Dakar.

field measurements (e.g. Tanré *et al.*, 2003; McConnell *et al.*, 2008; Osborne *et al.*, 2008; Schladitz *et al.*, 2009). There is however a small disparity between the AERONET single-scattering albedos at Banizoumbou and the models. The Banizoumbou data give single-scattering albedos of only 0.91, 0.03 lower than those at Dakar, mainly due to a higher imaginary component to the refractive index in the Banizoumbou retrievals. This would imply either a different mineral composition or mixing with carbonaceous aerosol, neither of which would have been represented in the model. Such variation is not represented in CAM, and the optical

properties varied little across the domain, hence we only show the regional mean.

The CAM-LN model gives good agreement with the observed specific extinction coefficients (k_{ext}) whereas the CAM-H k_{ext} values are 30–50% lower than observed because of the greater proportion of coarse particles (size bin 5, see Figure 14). Values of k_{ext} in CAM-H also remained lower than observed values in regions more remote from sources (e.g. Cape Verde, results not shown) showing that this low bias was not an artefact of the averaging region. Getting the ratio between AOD and mass loading, as expressed via k_{ext} , is important since the dust model is typically validated

Table II. Aerosol optical properties from CAM model, AERONET retrievals and FAAM aircraft measurements at 440, 550 and 675 nm

	$k_{\text{ext } 550} \text{ (m}^2 \text{ g}^{-1}\text{)}$	$\omega_{440, 550, 675}$	$\hat{A}_{440-675}$	g_{550}
<i>GERBILS region</i>				
CAM-H	0.28	0.92, 0.94, 0.95	0.0	0.75
CAM-LN	0.41	0.94, 0.95, 0.96	0.1	0.74
FAAM	0.48 ^a , 0.44 ^b	0.95 ^a , 0.97, 0.98 ^a	−0.1	0.73 ^a , 0.73 ^b
AERONET-Dakar	0.56	0.91, 0.94, 0.97	0.1	0.76
AERONET-Baniz	0.49	0.88, 0.91, 0.95	0.1	0.75

^aMie and

^bT-Matrix calculations based on the FAAM campaign mean size distribution.

k_{ext} is specific extinction coefficient, ω single scattering albedo, \hat{A} Ångström exponent and g asymmetry parameter.

and tuned with AOD observations, but users may also be required to give information on the mass loading. Hence we rely on the model having realistic k_{ext} values at $0.55 \mu\text{m}$ to ensure that both AODs and mass concentrations are realistic. In conclusion, these results show that specifying a size distribution at source (as in CAM-LN) ensures good aerosol optical properties and this seemed a more successful strategy in these simulations. However, with further tuning and improvements to surface characteristics and/or the uplift formulation, the CAM-H approach may prove a more realistic and skilful method.

7. Vertical distributions

The vertical distribution of dust is important as it governs the interaction of dust with long-wave and short-wave radiation and determines the impact on atmospheric visibility as a function of altitude. The FAAM aircraft made a total of 35 profiles during GERBILS, all of which have been compared with co-located CAM data. In Figure 15 we show a selection of three examples and the mean profile, averaged over all 35 individual profiles. The aircraft profiles show the nephelometer scattering at $0.55 \mu\text{m}$ as this provides the most relevant measure of the dust in relation to visibility and short-wave AOD. The model aerosol scattering coefficient was calculated from the mass mixing ratio profiles for each dust bin and the values of specific scattering coefficient at $0.55 \mu\text{m}$ from CAM's radiation scheme (Edwards and Slingo, 1996).

The models reproduced the observed vertical distribution of dust very well in many cases, as exemplified by Figure 15(a) and (b), and characterize the depth of the Saharan air layer very well ($\sim 6 \text{ km}$). In some cases the models produced too much dust at altitudes below 2 km, as shown in Figure 15(b), and this bias is also reflected in the campaign mean (Figure 15(d)). The model also missed dust events on some occasions, as shown by Figure 15(c). This particular profile corresponds to the dust event over southern Mali examined in section 3.2. In this case the dust plumes in the models were simply not far enough south at the time of observation (see Figure 5). Both models tend to produce similar results and on average they reproduce the campaign mean vertical distribution of dust very well, except for the overestimation near the surface. This discrepancy may be influenced to a certain extent by losses in the Rosemount inlet used to draw the aerosol sample into the nephelometer (see Johnson and Osborne, 2011, for further details). Such losses could be greater at lower altitudes if large particles were preferentially concentrated in that height range. However, the SID2 probe showed no consistent variation of the aerosol size distribution between low (0–2 km) and medium altitude (2–6 km) layers. Therefore we conclude that the discrepancy is unlikely to be entirely an artefact of the observations and could be due to insufficient vertical mixing in the CAM between the local boundary layer and the residual layer above.

8. Radiative effects of dust

The influence of dust on the radiation budget was determined by comparing modelled radiation fields against a dust-free, but otherwise identical, CAM simulation. The model data were screened to avoid cloudy pixels and AOD

< 0.05 . The effects of dust on short-wave and long-wave radiation were then calculated at the top of the atmosphere (TOA) and surface. Radiative efficiencies were also calculated as the radiative effect of dust divided by the $0.55 \mu\text{m}$ AOD. Figure 16 shows an example of TOA radiative efficiencies and the corresponding AOD field for 1200 UTC on 18 June 2007. The short-wave TOA radiative effect is strong and negative ($\sim -100 \text{ W m}^{-2}$ per AOD) over the ocean but small and either positive or negative over land (-40 to 60 W m^{-2} per AOD). This illustrates the important influence of surface albedo on the sign and magnitude of short-wave TOA radiative effects for partially absorbing aerosol. The long-wave TOA radiative effect is positive everywhere but also varies considerably between ocean (10 to 20 W m^{-2} per AOD) and land (30 to 60 W m^{-2} per AOD). This land/sea contrast is due mainly to differences between ocean and daytime land surface temperatures.

To evaluate these model results, we compare against flight measurements made on 18 June 2007 off the west coast of Africa (flight plans are detailed in Haywood *et al.* (2011)). This flight included a long run at an altitude of 7.5 km running southwards over the ocean about 100 km west of the African coastline. Visual and radiometer observations suggest virtually aerosol-free conditions to the north of 22.5°N and an increase in dust to the south of that point. These observations correspond well to the model AOD field (Figure 16(a)) that shows dust AOD < 0.05 along the west coast of Africa until 22°N , south of which is a large dust plume. Using broadband radiometers, Haywood *et al.* inferred an increase of $33 \pm 3 \text{ W m}^{-2}$ in outgoing short-wave radiation at 7.5 km between the dust-free area and a region above the dust plume. A nephelometer profile through the same section of the dust plume indicated an AOD of 0.46 ± 0.1 at $0.55 \mu\text{m}$. Hence the dust is estimated to have a radiative efficiency of $-71 \pm 15 \text{ W m}^{-2}$. Surface radiative effects were determined by a run at 100 ft (30 m) altitude beneath the same section of dust plume. All results are listed in Table III. For comparison, model fields were averaged over a 50 km by 100 km box centred over the aircraft measurement pattern (20 – 21°N , 17.5 – 18°W) between 1600 and 1700 UTC, corresponding to the time of the measurements. The model AODs are both reasonably close to the aircraft value (0.52, 0.34, and 0.46 for CAM-H, CAM-LN and FAAM respectively).

The TOA short-wave effects differ between the models but this is mainly due to differing AODs, therefore it is more instructive to compare radiative efficiencies, and actually these are very similar (-109 , -113 W m^{-2}). However, these are about 50% higher than the forcing efficiency inferred from the aircraft observations (71 W m^{-2}). The cause of this discrepancy is not clear. High-resolution (220 band) single-column radiative transfer calculations based on the aircraft measurements suggested efficiencies of around -100 W m^{-2} (Haywood *et al.*, 2011). These lend support to the CAM results but do not explain the discrepancy with the observationally inferred radiative efficiency. The surface short-wave efficiencies are of a slightly higher magnitude (-146 , -152 W m^{-2}) due to the combined effects of scattering and absorption within the atmosphere that both attenuate downwelling short-wave radiation.

The long-wave effects are generally smaller than the short-wave effects but always positive since the dust acts in a similar manner to a greenhouse gas or tenuous cloud layer. This means increases of 17 to 21 W m^{-2} per AOD at TOA and

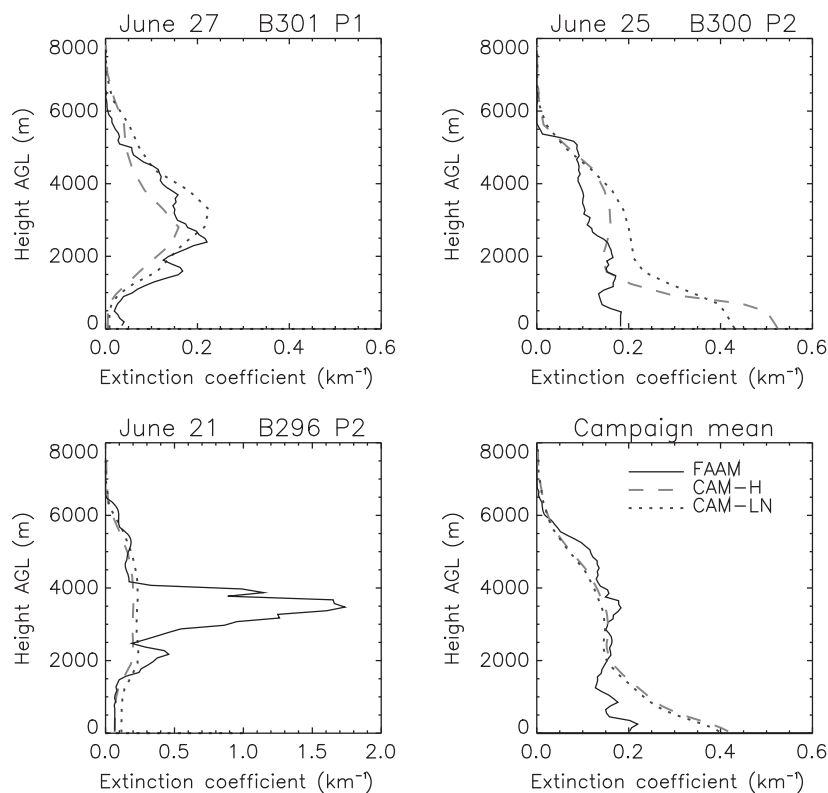


Figure 15. Aerosol extinction coefficient as a function of height above ground level from FAAM aircraft profiles and the CAM models. Profiles were located at: 13.9°N, 1.6°W (B301 P1), 18.0°N, 7.8°W (B300 P2), 13.0°N, 8.5°W (B296 P2).

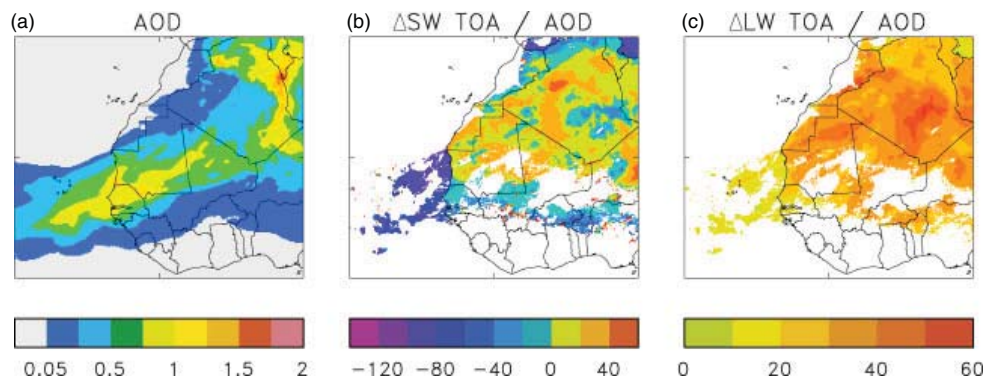


Figure 16. (a) AOD at $0.55 \mu\text{m}$ and the change in TOA (b) short-wave and (c) long-wave radiative efficiency due to dust from the CAM-LN model at 1200 UTC on 18 June 2007. This figure is available in colour online at wileyonlinelibrary.com/journal/qj

27 to 31 W m^{-2} per AOD at the surface (see Table III). The long-wave efficiency is slightly higher for CAM-LN than CAM-H, not because of differences in size distribution but because CAM-H had a higher aerosol amount and there is some saturation in the long-wave response to increased concentration of dust.

9. Conclusions

The Met Office CAM was used to produce dust forecasts in support of the GERBILS campaign. The dust scheme originating from the Hadley Centre climate model and has been adapted for use in operational weather forecast models. The GERBILS experiment offered an opportunity to evaluate the performance of the dust scheme against intensive aircraft

observations and remote-sensing retrievals from satellite and AERONET.

The CAM model was able to produce many of the basic features of dust uplift and transport throughout the observation period. The large-scale dust storm that occurred on 21 June 2007 was captured in a fairly realistic manner showing an appropriate response to synoptically driven high-wind events. However, comparisons against aircraft profiles, AERONET time series and MODIS AOD products showed the dust plume to be too far north in the model, both during this event and in the campaign mean field. This reflects errors in the geographic distribution of dust sources and the need for a better representation of mesoscale and subgrid-scale dynamical processes. A comparison against observed dust sources showed that dust emissions in the

Table III. Radiative effects ($W m^{-2}$) and AODs at $0.55 \mu m$ for a case-study over ocean

	AOD	ΔSW_{TOA}	ΔSW_{TOA} /AOD	ΔSW_{SFC}	ΔSW_{SFC} /AOD	ΔLW_{TOA}	ΔLW_{TOA} /AOD	ΔLW_{SFC}	ΔLW_{SFC} /AOD
FAAM ^a	0.46	-33	-72	-47	-102	8	18	16	35
CAM-H	0.52	-57	-109	-76	-146	9	17	15	27
CAM-LN	0.34	-38	-113	-51	-152	7	21	11	31

^aTOA estimates from FAAM are approximated from measurements at 7.5 km. Surface (SFC) estimates from FAAM are approximated from 30 m over ocean.

model did not extend far enough south into the Sahel. Further analysis showed that the clay fraction term in the dust uplift formulation did not adequately describe the geographic distribution of dust sources over the Sahara. Whether this is due to deficiencies in the input dataset or limitations in the uplift formulation is an area for future work. A comparison of the vegetation fraction in the CAM-H with the annual mean dust source observations also highlights the poor representation of the die-back of seasonal vegetation in the dust uplift, which could be rectified by including either seasonally varying vegetation fractions or the use of information such as the seasonally varying leaf-area index.

Individual dust sources are often small-scale features; ephemeral lake and river beds (e.g. Gillette, 1999; Prospero *et al.*, 2002; Mahowald *et al.*, 2003; Zender *et al.*, 2003b; Washington *et al.*, 2006; Schepanski *et al.*, 2009), and it may be that a more complex approach is required which uses both large-scale soil information, such as the clay fraction and seasonally corrected vegetation fractions, in conjunction with more detailed information about smaller-scale features to produce a preferential source term representing the availability of erodible soil/sediment at the surface (e.g. Ginoux *et al.*, 2001; Liu *et al.*, 2003; Zender *et al.*, 2003b; Grini *et al.*, 2005), as already tested by Ackerley *et al.* (2009) in a lower-resolution version of the Met Office Unified Model.

The aerosol size distributions and short-wave optical properties compared well with aircraft and AERONET data from the GERBILS experiment. This led to realistic interactions with short-wave and long-wave radiation that were generally consistent with aircraft radiometric measurements and high-resolution off-line radiative transfer calculations based on the GERBILS observations. Better size distributions and extinction coefficients were achieved when specifying the size distribution of dust entering the atmosphere rather than predicting it from size-dependent threshold friction velocities. This showed that the approach of specifying the size distribution seemed the most practical and reliable in this forecasting application. In other contexts, such as climate change experiments, this fixed approach may not be appropriate since the emitted size distribution should vary with physical processes and changes in surface characteristics. However, as shown in this analysis, adopting the dynamic approach is more difficult as it increases the sensitivity of the dust loading and optical properties to other model errors, and uncertainties in tuneable parameters. In most instances the model did a good job at vertical transport and mixing of dust, as shown by comparisons with aircraft profiles. However, there was a shortfall in the long-range transport of dust across the Atlantic, indicating that dry deposition may occur too quickly in the model.

Acknowledgements

The FAAM aircraft is jointly funded by the Met Office and the Natural Environmental Research Council. We thank NASA Goddard Space Flight Center and AERONET site managers for provision of the AERONET data.

References

- Ackerley D, Highwood EJ, Harrison MAJ, McConnell CL, Joshi MM, Walters DN, Milton SF, Greed G, Brooks ME. 2009. The development of a new dust uplift scheme in the Met Office Unified ModelTM. *Meteorol. Appl.* **16**: 445–460.
- Alfaro SC, Gomes L. 2001. Modeling mineral aerosol production by wind erosion: Emission intensities and aerosol size distributions in source areas. *J. Geophys. Res.* **106**: 18075–18084.
- Bagnold RA. 1941. *The Physics of Blown Sand and Desert Dunes*, p 265. Methuen: New York. Reprinted by Dover Publications, 2005.
- Balkanski Y, Schulz M, Claquin T, Guibert S. 2007. Reevaluation of mineral aerosol radiative forcings suggests a better agreement with satellite and AERONET data. *Atmos. Chem. Phys.* **7**: 81–95.
- Bou Karam D, Flamant C, Knippertz P, Reitebuch O, Pelon J, Chong M, Dabas A. 2008. Dust emissions over the Sahel associated with the West African monsoon intertropical discontinuity region: A representative case-study. *Q. J. R. Meteorol. Soc.* **134**: 621–634.
- Bou Karam D, Flamant C, Tulet P, Todd MC, Pelon J, Williams E. 2009. Dry cyclogenesis and dust mobilization in the intertropical discontinuity of the West African monsoon: A case study. *J. Geophys. Res.* **114**: D05115, DOI: 10.1029/2008JD010952.
- Brown AR, Beare RJ, Edwards JM, Lock AP, Keogh SJ, Milton SF, Walters DN. 2008. Upgrades to the boundary-layer scheme in the Met Office numerical weather prediction model. *Boundary-Layer Meteorol.* **128**: 117–132.
- Christopher SA, Gupta P, Haywood JM, Greed G. 2008. Aerosol optical thicknesses over North Africa: 1. Development of a product for model validation using Ozone Monitoring Instrument Multiangle Imaging Spectroradiometer and Aerosol Robotic Network. *J. Geophys. Res.* **113**: D00C04, DOI: 10.1029/2007JD009446.
- Cope ME, Hess GD, Lee S, Tory K, Azzi M, Carras J, Lilley W, Manins PC, Nelson P, Ng L, Puri K, Wong N, Walsh S, Young M. 2004. The Australian air quality forecasting system. Part I: Project description and early outcomes. *J. Appl. Meteorol.* **43**: 649–662.
- d'Almeida GA. 1987. On the variability of desert aerosol radiative characteristics. *J. Geophys. Res.* **92**: 3017–3026.
- Dharssi I, Vidale PL, Verhoef A, Macpherson B, Jones CP, Best M. 2010. 'New soil physical properties implemented in the Unified Model at PS18.' Met R&D Technical Report 528. Met Office, Exeter, UK.
- Dubovik O, Sinyuk A, Lapyonok T, Holben BN, Mishchenko M, Yang P, Eck TF, Volten H, Muñoz O, Veihelmann B, van der Zande WJ, Leon J-F, Sorokin M, Slutsker I. 2006. Application of spheroid models to account for aerosol particle nonsphericity in remote sensing of desert dust. *J. Geophys. Res.* **111**: D11208, DOI: 10.1029/2005JD006619.
- Edwards JM, Slingo A. 1996. Studies with a flexible radiation code. I: Choosing a configuration for a large-scale model. *Q. J. R. Meteorol. Soc.* **122**: 689–719.
- FAO/IIASA/ISRIC/ISS-CAS/JRC. 2008. *Harmonised world soil database (version 1.0)*. FAO: Rome, Italy and IIASA: Laxenburg, Austria.
- Fécan F, Marticorena B, Bergametti G. 1999. Parametrization of the increase of the aeolian erosion threshold wind friction velocity due to soil moisture for arid and semi-arid areas. *Ann. Geophys.* **17**: 149–157.
- Gillette DA. 1979. Environmental factors affecting dust emission by wind erosion, Chapter 4 in *Saharan Dust*, Morales C (ed). John Wiley: New York, NY.

- Gillette DA. 1999. A qualitative geophysical explanation for 'hot spot' dust emitting source regions. *Beitr. Phys. Atmos.* **72**: 67–77.
- Ginoux P, Chin M, Tegen I, Prospero JM, Holben B, Dubovik O, Lin S.-J. 2001. Sources and distributions of dust aerosols simulated with the GOCART model. *J. Geophys. Res.* **106**: 20255–20273.
- Global Soil Data Task Group. 2000. Global Gridded Surfaces of Selected Soil Characteristics (IGBP-DIS). (International Geosphere–Biosphere Programme – Data and Information System). Dataset. Available online at <http://www.daac.ornl.gov>. Oak Ridge National Laboratory Distributed Active Archive Center, Oak Ridge, Tennessee, USA. DOI: 10.3334/ORNDAAC/569.
- Greed G, Haywood JM, Milton SF, Keil A, Christopher S, Gupta P, Highwood EJ. 2008. Aerosol optical depths over North Africa: 2. Modeling and model validation. *J. Geophys. Res.* **113**: D00C05, DOI: 10.1029/2007JD009457.
- Gregory D, Rowntree PR. 1990. A mass flux convection scheme with representation of cloud ensemble characteristics and stability-dependent closure. *Mon. Weather Rev.* **118**: 1483–1506.
- Grini A, Myhre G, Zender CS, Isaksen ISA. 2005. Model simulations of dust sources and transport in the global atmosphere: Effects of soil erodibility and wind speed variability. *J. Geophys. Res.* **110**: D02205, DOI: 10.1029/2004JD005037.
- Haywood JM, Allan RP, Culverwell I, Slingo A, Milton SF, Edwards J, Clerbaux N. 2005. Can desert dust explain the outgoing longwave radiation anomaly over the Sahara during July 2003? *J. Geophys. Res.* **110**: D05105, DOI: 10.1029/2004JD005232.
- Haywood JM, Johnson BT, Osborne SR, Mulcahy J, Brooks ME, Harrison M, Milton SF, Brindley H. 2011. Observations and modelling of the solar and terrestrial radiative effects of Saharan dust: a radiative closure case-study over oceans during the GERBILS campaign. *Q. J. R. Meteorol. Soc.* **137**: 1211–1226, DOI: 10.1002/qj.770.
- Heinold B, Tegen I, Schepanski K, Hellmuth O. 2008. Dust radiative feedback on Saharan boundary layer dynamics and dust mobilization. *Geophys. Res. Lett.* **35**: L20817, DOI: 10.1029/2008GL03519.
- Hollingsworth A. 2005. 'The GEMS project – making a contribution to the environmental monitoring mission of ECMWF.' *ECMWF Newsletter* **103**: 17–20.
- Hsu NC, Tsay S.-C, King MD, Herman JR. 2004. Aerosol properties over bright-reflecting source regions. *IEEE Trans. Geosci. Remote Sensing* **42**: 557–569.
- Johnson BT, Osborne SR. 2011. Physical and optical properties of mineral dust aerosol measured by aircraft during the GERBILS campaign. *Q. J. R. Meteorol. Soc.* **137**: 1117–1130, DOI: 10.1002/qj.777.
- Klaver A, Formenti P, Caquingue S, Chevaillier S, Auset P, Calzolari G, Osborne S, Johnson B, Harrison M, Dubovik O. 2011. Physico-chemical and optical properties of Sahelian and Saharan mineral dust: *in situ* measurements during the GERBILS campaign. *Q. J. R. Meteorol. Soc.* **137**: 1193–1210, DOI: 10.1002/qj.889.
- Knippertz P, Deutscher C, Kandler K, Müller T, Schulz O, Schütz L. 2007. Dust mobilization due to density currents in the Atlas region: Observations from the Saharan Mineral Dust Experiment 2006 field campaign. *J. Geophys. Res.* **112**: D21109, DOI: 10.1029/2007JD008774.
- Knyazikhin Y, Glassy J, Privette JL, Tian Y, Lotsch A, Zhang Y, Wang Y, Morisette JT, Votava P, Myneni RB, Nemani RR, Running SW. 1999. 'MODIS Leaf Area Index (LAI) and Fraction of Photosynthetically Active Radiation absorbed by vegetation (FPAR) product (MOD15) algorithm theoretical basis document.' NASA Goddard Space Flight Center: Greenbelt, MA, USA.
- Koch J, Renno NO. 2005. The role of convective plumes and vortices on the global aerosol budget. *Geophys. Res. Lett.* **32**: L18806, DOI: 10.1029/2005GL023420.
- Levy RC, Remer LA, Mattoo S, Vermote EF, Kaufman YJ. 2007. Second-generation operational algorithm: Retrieval of aerosol properties over land from inversion of Moderate Resolution Imaging Spectroradiometer spectral reflectance. *J. Geophys. Res.* **112**: D13211, DOI: 10.1029/2006JD007811.
- Liu M, Westphal DL, Wang S, Shimizu A, Sugimoto N, Zhou J, Chen Y. 2003. A high-resolution numerical study of the Asia dust storms of April 2001. *J. Geophys. Res.* **108**: 8653, DOI: 10.1029/2002JD003178.
- Liu M, Westphal DL, Walker AL, Holt TR, Richardson KA, Miller SD. 2007. COAMPS real-time dust storm forecasting during Operation Iraqi Freedom. *Weather and Forecasting* **22**: 192–206.
- Loveland TR, Belward AS. 1997. The IGBP-DIS global 1 km land cover data set, DISCover: First results. *Int. J. Remote Sensing* **18**: 3289–3295.
- McConnell CL, Highwood EJ, Coe H, Formenti P, Anderson B, Osborne SR, Nava S, Desboeufs K, Chen G, Harrison MAJ. 2008. Seasonal variations of the physical and optical characteristics of Saharan dust: Results from the Dust Outflow and Deposition to the Ocean (DODO) experiment. *J. Geophys. Res.* **113**: D14S05, DOI: 10.1029/2007JD009606.
- Mahowald NM, Bryant RG, del Corral J, Steinberger L. 2003. Ephemeral lakes and desert dust sources. *Geophys. Res. Lett.* **30**: 1074, DOI: 10.1029/2002GL016041.
- Marshall JH, Parker DJ, Grams CM, Taylor CM, Haywood JM. 2008a. Uplift of Saharan dust south of the intertropical discontinuity. *J. Geophys. Res.* **113**: D21102, DOI: 10.1029/2008JD009844.
- Marshall JH, Parker DJ, Grams CM, Johnson BT, Grey WMF, Ross AN. 2008b. Observations of mesoscale and boundary-layer scale circulations affecting dust transport and uplift over the Sahara. *Atmos. Chem. Phys.* **8**: 6979–6993.
- Marticorena B, Bergametti G. 1995. Modeling the atmospheric dust cycle: 1. Design of a soil-derived dust emission scheme. *J. Geophys. Res.* **100**: 16415–16430.
- Marticorena B, Chatenet B, Rajot JL, Traoré S, Coulibaly M, Diallo A, Koné I, Maman A, NDiaye T, Zakou A. 2010. Temporal variability of mineral dust concentrations over West Africa: Analyses of a pluriannual monitoring from the AMMA Sahelian Dust Transect. *Atmos. Chem. Phys. Discuss.* **10**: 8051–8101.
- Martin GM, Ringer MA, Pope VD, Jones A, Dearden C, Hinton TJ. 2006. The physical properties of the atmosphere in the new Hadley Centre Global Environmental Model (HadGEM1). Part I: Model description and global climatology. *J. Climate* **19**: 1274–1301.
- Miller DA, White RA. 1998. A continuous United States multilayer soil characteristics dataset for regional climate and hydrology modeling. *Earth Interact.* **2**: 1–26.
- Milton SF, Greed G, Brooks ME, Haywood JM, Johnson BT, Allan RP, Slingo A, Grey WMF. 2008. Modeled and observed atmospheric radiation balance during the West African dry season: Role of mineral dust, biomass burning aerosol, and surface albedo. *J. Geophys. Res.* **113**: D00C02, DOI: 10.1029/2007JD009741.
- Nickovic S, Kallos G, Papadopoulos A, Kakaliagou O. 2001. A model for prediction of desert dust cycle in the atmosphere. *J. Geophys. Res.* **106**: 18113–18129.
- Osborne SR, Johnson BT, Haywood JM, Baran AJ, Harrison MAJ, McConnell CL. 2008. Physical and optical properties of mineral dust aerosol during the Dust and Biomass-burning Experiment. *J. Geophys. Res.* **113**: D00C03, DOI: 10.1029/2007JD009551.
- Park S.-U, In H.-J. 2003. Parameterization of dust emission for the simulation of the yellow sand (Asian dust) event observed in March 2002 in Korea. *J. Geophys. Res.* **108**: 4618, DOI: 10.1029/2003JD003484.
- Prospero JM, Ginoux P, Torres O, Nicholson SE, Gill TE. 2002. Environmental characterization of global sources of atmospheric soil dust identified with the NIMBUS 7 Total Ozone Mapping Spectrometer (TOMS) absorbing aerosol product. *Rev. Geophys.* **40**: 1002, DOI: 10.1029/2000RG000095.
- Remer LA, Kaufman YJ, Tanré D, Mattoo S, Chu DA, Martins JV, Li R.-R, Ichoku C, Levy RC, Kleidman RG, Eck TF, Vermote E, Holben BN. 2005. The MODIS aerosol algorithm, products, and validation. *J. Atmos. Sci.* **62**: 947–973.
- Rodwell M. 2005. 'The local and global impact of the recent change in model aerosol climatology.' *ECMWF Newsletter* **105**: 17–23.
- Schepanski K, Tegen I, Laurent B, Heinold B, Macke A. 2007. A new Saharan dust source activation frequency map derived from MSG-SEVIRI IR-channels. *Geophys. Res. Lett.* **34**: L18803, DOI: 10.1029/2007GL030168.
- Schepanski K, Tegen I, Todd MC, Heinold B, Bönisch G, Laurent B, Macke A. 2009. Meteorological processes forcing Saharan dust emission inferred from MSG-SEVIRI observations of subdaily dust source activation and numerical models. *J. Geophys. Res.* **114**: D10201, DOI: 10.1029/2008JD010325.
- Schladitz A, Müller T, Kaaden N, Massling A, Kandler K, Ebert M, Weinbruch S, Deutscher C, Wiedensohler A. 2009. *In situ* measurements of optical properties at Tinfou (Morocco) during the Saharan Mineral Dust Experiment SAMUM 2006. *Tellus* **61B**: 64–78.
- Shao Y, Yang Y, Wang J, Song Z, Leslie LM, Dong C, Zhang Z, Lin Z, Kanai Y, Yabuki S, Chun Y. 2003. Northeast Asian dust storms: Real-time numerical prediction and validation. *J. Geophys. Res.* **108**: 4691, DOI: 10.1029/2003JD003667.
- Tanaka TY, Orito K, Sekiyama TT, Shibata K, Chiba M, Tanaka H. 2003. MASINGAR, a global tropospheric aerosol chemical transport model coupled with MRI/JMA98 GCM: Model description. *Pap. Meteorol. Geophys.* **53**: 119–138.
- Tanré D, Haywood JM, Pelon J, Léon JF, Chatenet B, Formenti P, Francis P, Goloub P, Highwood EJ, Myhre G. 2003. Measurement and modeling of the Saharan dust radiative impact: Overview of the Saharan Dust Experiment (SHADE). *J. Geophys. Res.* **108**: 8574, DOI: 10.1029/2002JD003273.
- Tegen I, Fung I. 1994. Modeling of mineral dust in the atmosphere: Sources, transport, and optical thickness. *J. Geophys. Res.* **99**: 22897–22914.

- Todd MC, Washington R, Martins JV, Dubovik O, Lizcano G, M'Bainayel S, Engelstaedter S. 2007. Mineral dust emission from the Bodélé Depression, northern Chad, during BoDEx 2005. *J. Geophys. Res.* **112**: D06207, DOI: 10.1029/2006JD007170.
- Tompkins AM, Cardinali C, Morcrette J-J, Rodwell M. 2005. Influence of aerosol climatology on forecasts of the African Easterly Jet. *Geophys. Res. Lett.* **32**: L10801, DOI: 10.1029/2004GL022189.
- Uno I, Satake S, Carmichael GR, Tang Y, Wang Z, Takemura T, Sugimoto N, Shimizu A, Murayama T, Cahill TA, Cliff S, Uematsu M, Ohta S, Quinn PK, Bates TS. 2004. Numerical study of Asian dust transport during the springtime of 2001 simulated with the Chemical Weather Forecasting System (CFORS) model. *J. Geophys. Res.* **109**: D19S24, DOI: 10.1029/2003JD004222.
- Uno I, Wang Z, Chiba M, Chun YS, Gong SL, Hara Y, Jung E, Lee S-S, Liu M, Mikami M, Music S, Nickovic S, Satake S, Shao Y, Song Z, Sugimoto N, Tanaka T, Westphal DL. 2006. Dust model intercomparison (DMIP) study over Asia: Overview. *J. Geophys. Res.* **111**: D12213, DOI: 10.1029/2005JD006575.
- Washington R, Todd MC, Lizcano G, Tegen I, Flamant C, Koren I, Ginoux P, Engelstaedter S, Bristow CS, Zender CS, Goudie AS, Warren A, Prospero JM. 2006. Links between topography, wind, deflation, lakes and dust: The case of the Bodélé Depression, Chad. *Geophys. Res. Lett.* **33**: L09401, DOI: 10.1029/2006GL025827.
- Woodward S. 2001. Modeling the atmospheric life cycle and radiative impact of mineral dust in the Hadley Centre climate model. *J. Geophys. Res.* **106**: 18155–18166.
- Zender CS, Bian H, Newman D. 2003a. Mineral Dust Entrainment And Deposition (DEAD) model: Description and 1990s dust climatology. *J. Geophys. Res.* **108**: 4416, DOI: 10.1029/2002JD002775.
- Zender CS, Newman D, Torres O. 2003b. Spatial heterogeneity in aeolian erodibility: Uniform, topographic, geomorphic, and hydrologic hypotheses. *J. Geophys. Res.* **108**: 4543, DOI: 10.1029/2002JD003039.